

Viscosity ratio across interfaces controls the stability and self-assembly of microrollers

Blaise Delmotte*

LadHyX, CNRS, Ecole Polytechnique, Institut Polytechnique de Paris, 91120 Palaiseau, France

We investigate the individual and collective dynamics of torque-driven particles, called microrollers, near fluid-fluid interfaces. We find that the viscosity ratio across the interface controls the speed and direction of the particles, their relative motion, the growth of a fingering instability and the self-assembled motile structures that emerge from it. By combining theory and large scale numerical simulations, we show how the viscosity ratio across the interface governs the long-range hydrodynamic interactions between particles and thus their collective behavior.

The motion of small driven particles near interfaces is observed in numerous biological and artificial systems [1–3]. Examples include droplets filled with self-propelled particles, where hydrodynamic couplings between the particles and the surrounding fluid-fluid interface induce collective motion and translation of the droplet [4–9]. Navigation near interfaces also happens in natural environments with air-water interfaces, such as marine foams [10] or films [11–13], and in biomedical environments where microswimmers move near soft vessel walls, visco-elastic media (biofilms, gels, tissues) or mucus layers [14–16].

Among them, spinning particles, such as torque-driven colloids (also called microrollers), use rotation-translation couplings near surfaces to self-propel. Synthetic microrollers are actuated by an external magnetic field rotating about an axis parallel to the interface. The orientation of the magnetic field can be varied over time to guide these particles in a variety of environments. Thanks to their steerability and to the strong long-range flows they generate, they offer promising perspectives for particle micromanipulation, fluid pumping and drug delivery in microfluidic and biological systems [17–24]. Above a rigid wall, hydrodynamic interactions between microrollers induce a variety of collective motions such as periodic leapfrog orbits [25, 26], the formation of fast moving layers [27–29], the emergence of dense fronts [30] and the growth of a fingering instability that releases stable motile clusters [31, 32]. However, despite the rich and well documented dynamics observed above rigid boundaries, little is known about their collective behavior near interfaces.

In this Letter, we combine theory and large scale numerical simulations to investigate the dynamics of microrollers near fluid-fluid interfaces. We show how the viscosity ratio across the interface, denoted ξ hereinafter, modifies the flow around the spinning particles, with dramatic consequences on their individual and collective motion. At the individual level, we find that ξ controls the direction and speed of a single microroller. We then consider the dynamics of particle pairs and show that ξ acts as an order parameter that determines the existence of periodic orbits. At the collective level, we demonstrate that ξ controls both the growth rate of the finger-

ing instability initially observed above a no-slip surface, and the self-assembly process that leads to the emergence of motile clusters. We finally use these findings to outline new strategies for pumping and particle transport in microfluidic systems.

We consider the motion of small torque-driven spherical particles with radius a suspended in a fluid with dynamic viscosity η_{in} above a fluid-fluid interface (Fig. 1a). The outer fluid on the other side of the interface has dynamic viscosity η_{out} which can vary from zero (e.g. air) to $+\infty$ (a rigid wall). We denote $\xi = \eta_{out}/\eta_{in}$ the viscosity ratio between the two fluids across the interface. In this work we consider particles with large contact angles that are not adsorbed to the surface (such as paramagnetic beads above air/water surfaces [27]). In typical experiments the particles are micron-sized ($a = O(1)\mu\text{m}$) and suspended in water ($\eta_{in} = 10^{-3}\text{Pa}\cdot\text{s}$). They rotate in synchrony with an external magnetic field with frequency $f = O(10)\text{Hz}$ thanks to a magnetic torque aligned with the y -axis denoted τ . The corresponding capillary number is $\text{Ca} = \eta_{in}u/\sigma \approx 10^{-6} - 10^{-5}$, where $u = \omega a = 2\pi f a$ is the maximal fluid velocity, reached on the particle surface due to the no-slip condition, and $\sigma = O(10^{-2})\text{N/m}$ is the typical surface tension between the two phases. Owing to the very small value of Ca and to the small size of the particles, the interface can be considered as flat and nondeformable. In this limit, one can compute the flow field around the particles using the Green's function \mathbf{G} of the Stokes equations which, by linearity, is given by [33]:

$$\mathbf{G} = 1/(\xi + 1)\mathbf{G}^{FS} + \xi/(\xi + 1)\mathbf{G}^W \quad (1)$$

where \mathbf{G}^{FS} is the Green's function of a domain bounded by a flat free-surface and \mathbf{G}^W a domain bounded by a flat no-slip wall, both of which have known analytical expressions based on image systems [34, 35]. Changing ξ from 0 to $+\infty$ in (1) transitions smoothly from a free-surface to a no-slip wall.

Single particle motion. – Using the Faxen formulae for the motion of a spherical particle in a non-uniform flow [36], the far-field approximation of the self-induced velocity of a single microroller above the interface, is given by [37]

$$v_0(\xi, h/a) = \frac{1}{4} \left(\frac{a}{h}\right)^2 \left[-\frac{1}{\xi + 1} + \frac{\xi}{\xi + 1} \frac{1}{2} \left(\frac{a}{h}\right)^2 \right], \quad (2)$$

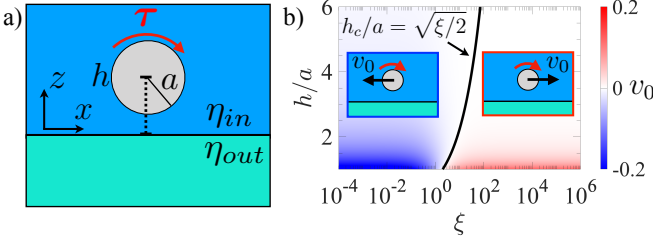


FIG. 1. a) Schematic of a torque-driven particle above a fluid-fluid interface. b) Self-induced velocity of the particle v_0 in response to a constant torque τ as a function of $\xi = \eta_{out}/\eta_{in}$ and normalized height h/a .

where the velocity has been normalized by $\tau/8\pi\eta a^2$. Interestingly, the sign of the velocity in (2) depends both on the viscosity ratio *and* the particle height (Fig. 1b). Below a critical value $\xi_c = 2$ the velocity is always negative, even though the applied torque is clockwise, and decays as $(a/h)^2$ for $\xi = 0$. This surprising backward motion has already been observed experimentally [27] and is due to the fact there is no velocity gradient on the free-surface underneath. The particle therefore experiences more viscous stress on its upper side, where velocity gradients are larger, than on the lower side. As a result, the particle “rolls” on the liquid above, which resists more against rotational motion, and thus moves backwards. When $\xi \geq \xi_c$, there is a critical height $h_c = \sqrt{\xi/2}a$ at which viscous stresses balance between both sides such that the particle rotates in place, i.e. $v_0(\xi > \xi_c, h_c) = 0$. v_0 is positive below h_c and negative above. In the limit of a no-slip wall, $\xi \rightarrow +\infty$, v_0 is always positive and decays as $(a/h)^4$. These results show that both the direction and speed of a rotating particle can be controlled with the viscosity ratio.

Pair dynamics.— When adding another particle in the system, the trajectories exhibit a richer dynamics than the individual motion described above: particles can follow a variety of periodic orbits, change direction or end up translating at a steady speed (Fig. 2a-c). We consider two torque-driven particles (denoted 1 and 2 respectively), lying in the (x, z) -plane vertical to the floor and separated by a distance $r_{12} = \sqrt{x_{12}^2 + z_{12}^2}$, where $x_{12} = x_1 - x_2$ and $z_{12} = z_1 - z_{12}$. For simplicity, we focus on the limit $a \ll \min(r_{12}, z_1, z_2)$, where the particles are considered as point-torques (rotlets) so that the equations of motion can be written compactly as a simple dynamical system with three degrees of freedom [37]:

$$\begin{bmatrix} \dot{x}_{12} \\ \dot{z}_{12} \\ \dot{z}_C \end{bmatrix} = \begin{bmatrix} 2z_{12} \left(\frac{1}{r_{12}^3} - \frac{\xi}{\xi+1} \frac{2x_{12}^2 - 4z_C^2}{R_{12}^5} \right) + \delta v_0 \\ 2x_{12} \left(\frac{1}{R_{12}^3} - \frac{1}{r_{12}^3} + \frac{\xi}{\xi+1} \frac{12z_C^2}{R_{12}^5} \right) \\ \frac{\xi}{\xi+1} \frac{6x_{12}z_{12}z_C}{R_{12}^5} \end{bmatrix} \quad (3)$$

where $z_C = (z_1 + z_2)/2$, and $R_{12} = \sqrt{x_{12}^2 + 4z_C^2}$. $\delta v_0 = -\frac{1}{4} \frac{1}{\xi+1} ((z_C + z_{12}/2)^{-2} - (z_C - z_{12}/2)^{-2})$ is the differ-

ence between the self-induced velocities in the point-particle limit. Here lengths have been rescaled by the initial height of the system $l_c = z_C^0 = z_C(t=0)$ and time by $t_c = 8\pi\eta l_c^3/\tau$. The dynamical system (3) has two critical saddle points with coordinates $\mathbf{x}_{\pm}^* = (x_{12} = \pm x_{12}^*, z_{12} = 0, z_C = 1)$, where $x_{12}^* \neq 0$ is a zero of $\dot{z}_{12}(x_{12}, 0, 1, \xi)$ [37].

These critical points separate periodic (leapfrog) and non-periodic orbits, as shown on Fig. 2b. Interestingly, their position, x_{12}^* , is controlled by the viscosity ratio ξ . To visualize this dependency, we examine the changes in the topology of the flow field around a spinning particle as a function of ξ (Fig. 2d). When $\xi = 0$ all the streamlines in the domain are closed and circular. As ξ increases, the region of closed streamlines contracts in the vicinity of the particle, while open streamlines, which push the fluid forward, occupy more space. To understand the effect of the flow on the periodicity of the orbits we place the particles at the critical point $x_{12} = x_{12}^*$ where $z_1 = z_2 = 1$ and we assume $x_1 > x_2$. At this position their relative, and thus absolute, vertical velocity vanishes $\dot{z}_{12} = 0 \Rightarrow \dot{z}_1 = \dot{z}_2 = \dot{z}_C = 0$. x_{12}^* therefore corresponds to the intersection between the contour of zero vertical velocity induced by a particle, $u_z = 0$, and the line $z = 1$ as shown on Fig. 2d. If $x_{12} > x_{12}^*$ then $\dot{z}_{12} > 0$ and the particles cannot perform the leapfrog motion, as can be intuited by superimposing the flow of

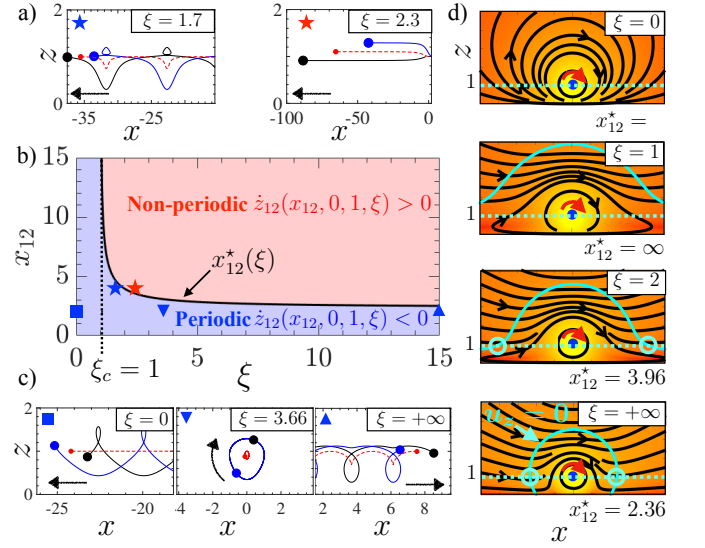


FIG. 2. a) Effect of ξ on the periodicity of trajectories of two rotlets (blue and black disks) with identical initial separation: $x_{12}^0 = 4$. Red disk and dashed line: position and trajectory of the center of mass (x_C, z_C) . Black arrow: direction of motion of x_C . b) Phase diagram of rotlet orbits near the critical points as a function of ξ and x_{12} . Black line: critical distance x_{12}^* . c) Effect of ξ on the direction of motion of a pair with $x_{12}^0 = 2$. d) Streamlines and flow field around a rotlet in the (x, z) -plane for various ξ . Cyan solid line: iso-value $u_z = 0$. Cyan dotted line: $z = 1$. Cyan circles: position of the critical horizontal separation x_{12}^* , reported below each panel.

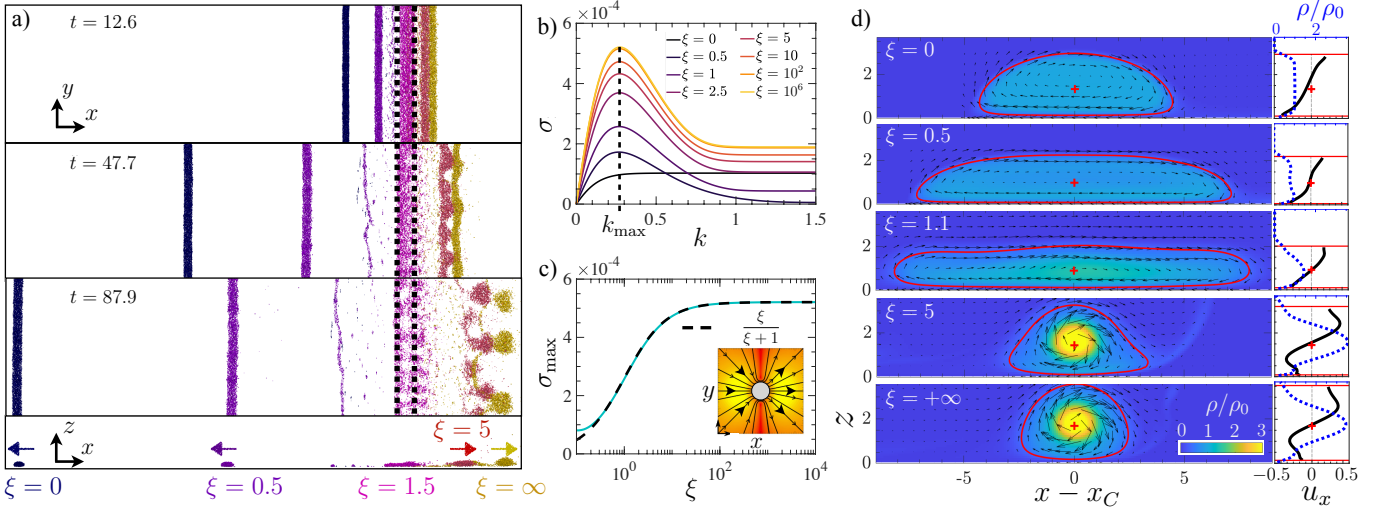


FIG. 3. a) Time-evolution of 10,000 microrollers initially uniformly distributed in a monolayer (delimited by the black dotted lines) above the interface. Each color corresponds to a different value of ξ simulated independently. Bottom panel: side view at $t = 87.9$. Arrows: direction of motion. b) Growth rate of the two line model (4)-(5) for various ξ . Dashed line: fastest growing mode k_{\max} . c) Maximum growth rate (solid cyan line) as a function of ξ . Dashed black line: prefactor $\sim \xi/(\xi + 1)$ due to the transverse flows generated above a no-slip boundary (inset). d) Particle density distribution $\rho(\mathbf{x}, t)$ obtained from (6)-(7) at $t = 1418$ (quasi-steady state) in the (x, z) -plane for various ξ . Black arrows: flow field. Solid red line: $\rho/\rho_0 = 0.4$. Red cross: position of the COM (x_C, z_C) . Side panels: density (dotted blue line) and velocity (solid black line) profiles at $x = x_C$.

two rotlets side by side (Fig. 2a and d). Below a critical value $\xi_c = 1$, \dot{z}_{12} is always negative at $z = 1$, which implies that there is no critical point x_{12}^* ($u_z = 0$ and $z = 1$ never meet) and thus that all the trajectories are periodic regardless of the initial separation (Fig. 2b-d). The viscosity ratio therefore controls the existence of periodic orbits. The viscosity ratio also sets the speed and direction of these periodic motions. In the limit $\xi = 0$ the backward motion is fastest and the height of the system remains constant ($\dot{z}_C = 0$) (Fig. 2c, left panel). Otherwise the direction of motion depends on the relative position of the particles so that, given an initial configuration, there is always a threshold value for which the pair orbits in place (e.g. $\xi = 3.66$ for $x_{12}^0 = 4$ in Fig. 2c, middle panel). In the limit $\xi = +\infty$, the pair always moves forward: $\dot{x}_C = 6z_C x_{12}^2 / R_{12}^5 > 0$ (Fig. 2c, right panel).

Collective dynamics.— We further explore the dynamics at the collective level where large collections of particles interact. In the rigid-wall limit ($\xi \rightarrow \infty$) the suspension exhibits a cascade of events: an initially uniform strip of particles forms a dense front which is subject to a transverse fingering instability, from which the fingertips then detach to generate dense motile structures. As shown in previous work, the wavelength at the onset of the instability is set by the mean height of the front [31, 32]. We investigate the effect of the viscosity ratio on this rich collective dynamics using large scale 3D Stokesian dynamics simulations that include both hydrodynamic and steric interactions between tens of thousands of microrollers above the interface [37]. Fig. 3a shows the time evolution of 10,000 microrollers initially

lying on a monolayer with area fraction $\phi = 0.65$, at a given height $z_C^0/a = 1.2$, for various viscosity ratios $\xi \in \{0, 0.5, 1.5, 5, +\infty\}$ (see SI movies). In the case of a no-slip wall, $\xi = +\infty$, the strips evolve as described above. The rollers inside the fingertips perform a treadmill motion that follows the clockwise rotation of the torque. A few particles are occasionally shed from the front and lifted up by flow of the rotating structures. When $\xi = 5$ the suspension behaves similarly with a slower forward motion. At a critical value $\xi \approx 1.5$, the suspension treads without translating, but the transverse instability still occurs in place, leading to a lateral separation of the particles, reminiscent of a Rayleigh-Plateau instability. Below that threshold, the suspension self-assembles into a long roll treading clockwise but moving backwards. When $\xi = 0.5$ the roll is wavy due to the transverse instability, but evolves at a significantly slower rate, and sporadically sheds particles from the rear. In the free-surface limit ($\xi = 0$), the transverse instability is suppressed and the roll remains straight and stable. It does not shed any particle because, as shown in the previous section, the streamlines of the flow induced by the microrollers are closed regardless of the separation distance (Fig. 2b, bottom panel). Finally, we note that the mean height of the particles in the fingertips slightly increases with ξ (Fig. 3a, bottom panel), which in turn increases the wavelength of the transverse instability. This is due to the upward advective flows ahead of the particles that get stronger with ξ (see (Fig. 2b) and allow the particles behind to lift the leading front where the instability occurs.

In order to better understand the effect of ξ on the transverse instability, we use a simple model consisting of two continuous lines of rotlets, \mathcal{L}_1 and \mathcal{L}_2 , separated by a distance d in a plane parallel to the interface at a constant height h . The lines are aligned along the y -axis with rotlet density $\rho_i(y, t)$ and position $x_i(y, t)$, $i = 1, 2$. The model is governed by the equations of motion of each line together with the conservation of rotlets along their length:

$$\begin{aligned} \frac{\partial x_i(y, t)}{\partial t} &= u_x(x_i(y, t), y) \\ \frac{\partial \rho_i(y, t)}{\partial t} &= -\frac{\partial[\rho_i(y, t)u_y(x_i(y, t), y)]}{\partial y}, \quad i = 1, 2, \end{aligned} \quad (4)$$

where length and time have been rescaled with $l_c = h$ and t_c defined above. The velocity (u_x, u_y) in the RHS arises from the long-ranged hydrodynamic interactions between the microrollers of each line, e.g.

$$u_x(\underbrace{x_i, y}_x) = \sum_{j=1}^2 \int_{-\infty}^{+\infty} \underbrace{\mu_x^{u\tau}(x_i - x_j, y - y')}_{x-x'} \rho_j(y') dy', \quad (5)$$

where $\mu_x^{u\tau}(\mathbf{x} - \mathbf{x}')$ is the x -component of the operator $\boldsymbol{\mu}^{u\tau}(\mathbf{x} - \mathbf{x}') = 1/2 (\nabla_{\mathbf{x}'} \times \mathbf{G}(\mathbf{x} - \mathbf{x}')) \cdot \mathbf{e}_y$ that computes the fluid velocity at position \mathbf{x} induced by a rotlet, directed along \mathbf{e}_y , at position \mathbf{x}' [37]. As shown in previous work, this model contains all the essential ingredients to faithfully reproduce the fingering instability above a no-slip wall [31] and naturally extends to fluid-fluid interfaces by using the linear combination of Green's functions in (1). The base state of this system corresponds to two straight lines with uniform rotlet densities ($\rho_i(y, t) = \rho_0$) translating at a steady speed, so that their position are constant in the moving frame ($x_1(y, t) = 0$, $x_2(y, t) = d$). After carrying a linear stability analysis of the system around the base state, we obtain an analytical expression for the growth rate $\sigma(k, \xi)$ [37], plotted on Fig. 3b. First, we notice that an identical fastest growing mode is selected for all values of ξ , as seen by the clear bump at $\lambda_{\max} = 2\pi/k_{\max} = 23$, except for $\xi = 0$ for which there is no clear selection. Second the corresponding growth rate, σ_{\max} , increases with ξ . The increase of σ_{\max} is quantified on Fig. 3c, and shows a plateau at large ξ . A detailed analysis of the two-line model shows that the growth rate of the transverse instability is proportional to the transverse flow u_y in (4). Since the microrollers do not induce transverse flows above a free surface ($u_y^{FS} = 0$ [37]), σ_{\max} scales as $\xi/(\xi + 1)$, which is the prefactor of the no-slip wall contribution \mathbf{G}^W in (1) (see inset of Fig. 3c). Overall the two-line model highlights the crucial role of these transverse flows and exhibits a good agreement with the large scale simulations in the sense that, for a given particle height, ξ only changes the growth rate of the instability without affecting much the dominant wavelength. However since the height of the particles is

kept constant in the model, it cannot capture the slight increase of the wavelength with ξ that is observed on Fig. 3a.

The nature of the interface does not only affect the direction of motion of the suspension and the growth of the transverse instability, but also the shape and structure of the emerging clusters. We study these changes from a macroscopic point of view, with a mean field description of the density of microrollers $\rho(\mathbf{x}, t)$ in the (x, z) -plane perpendicular to the interface, denoted \mathcal{P} . $\rho(\mathbf{x}, t)$ obeys the conservation equation

$$\frac{\partial \rho}{\partial t} + \nabla \cdot (\mathbf{u}\rho) = 0. \quad (6)$$

Similarly to (5), the velocities in the flux term arise from the long-ranged hydrodynamic interactions between microrollers, but here in the whole plane \mathcal{P} perpendicular to the interface, e.g.

$$u_x(\mathbf{x}, t) = \int_{\mathcal{P}} \mu_x^{u\tau}(\mathbf{x} - \mathbf{x}') \rho(\mathbf{x}', t) d\mathbf{x}'. \quad (7)$$

The nonlocal equations (6)-(7) are solved numerically [37] and the rollers are initially uniformly distributed ($\rho = \rho_0$) over a thin strip of aspect ratio $\gamma = L/H = 9.4$ near the interface. After some time, the system reaches a quasi-steady state where a main cluster emerges and translates at a steady speed (see SI Movies). Fig. 3d shows a snapshot of the microroller density at the same dimensionless time in the quasi-permanent regime for various values of ξ together with the density $\rho(x_C, z)$ and velocity profiles $u_x(x_C, z)$ at the central cross-section of the cluster. Here the cluster is delimited by the iso-value $\rho = 0.4\rho_0$ highlighted by a solid red line. As in the discrete particle simulations, the velocity of the cluster is fastest and backwards for $\xi = 0$, vanishes around $\xi \approx 1.1$, where the cluster treadmills in place, and increases forward beyond. The shape of the cluster evolves from a near-hemisphere of aspect ratio $\gamma = 3.1$ at $\xi = 0$, to a ‘‘pancake’’ shape ($\gamma = 8.4$) at $\xi = 1.1$, and becomes circular when ξ increases further ($\gamma = 2$ and $\gamma = 1.4$ for $\xi = 5$ and $\xi = +\infty$). In addition to the shape, ξ controls the particle distribution inside the cluster. The distribution is uniform at $\xi = 0$ ($\rho \approx \rho_0$) and becomes more peaked as ξ increases, with a maximum $\rho_{\max} \approx 3.8\rho_0$ reached at $\xi = +\infty$. These changes in concentration, together with the boundary condition at the interface underneath, determine the velocity profile within the cluster. At $\xi = 0$, the treadmilling motion is fastest near the bottom interface, where the slip condition allows for large velocities. As ξ increases, the particles concentrate at the center and the no-slip condition becomes stronger, which shifts the maximum velocity upwards and generates a rigid-body motion near the core.

Discussion.— In this Letter, we have shown that the viscosity ratio across the interface is a powerful parameter to control the individual and collective motion of

microrollers. It changes the direction and the speed of the particles, determines their relative trajectories, sets the growth of the fingering instability, and modifies the microstructure of the emerging clusters. Beyond these fundamental findings, our results open new perspectives for particle transport and pumping in biomedical and microfluidic environments. For instance, channel walls structured with air-filled grooves ($\xi = 0$) oriented perpendicular to the particles' motion could be used to pump fluid: due to the competition between forward motion on the solid floor and backward motion at the interfaces, large collections of microrollers would remain trapped near the grooves and generate strong pumping flows along the channel while spinning in place. Also, by using different fluids among the grooves, one could control the speed and travel time of the microrollers in a passive way, i.e. without monitoring them and changing their angular speed over time. Finally, in this work we considered particles lying *above* the interface with large contact angles. In some cases the particles wet the outer fluid and get adsorbed at the interface. Adsorbed active particle layers can be used as active surfactants to modulate interfacial properties in emulsions or films, or to pump and mix flows in the surrounding fluids [3, 38]. Up to now, the hydrodynamics of torque-driven particles straddling fluid-fluid interfaces is still not well-understood [39] and should deserve more attention given their exciting applications.

* blaise.delmotte@cnr.fr

- [1] E. Lauga, Annual Review of Fluid Mechanics **48**, 105 (2016).
- [2] C. Bechinger, R. Di Leonardo, H. Löwen, C. Reichhardt, G. Volpe, and G. Volpe, Reviews of Modern Physics **88**, 045006 (2016).
- [3] W. Fei, Y. Gu, and K. J. Bishop, Current opinion in colloid & interface science **32**, 57 (2017).
- [4] T. Gao and Z. Li, Physical Review Letters **119**, 108002 (2017).
- [5] B. Vincenti, G. Ramos, M. L. Cordero, C. Douarche, R. Soto, and E. Clement, Nature communications **10**, 1 (2019).
- [6] D. Singh, A. Domínguez, U. Choudhury, S. Kottapalli, M. N. Popescu, S. Dietrich, and P. Fischer, Nature communications **11**, 1 (2020).
- [7] Z. Huang, T. Otori, and T. Ishikawa, Physical Review E **102**, 022603 (2020).
- [8] M. Rajabi, H. Baza, T. Turiv, and O. D. Lavrentovich, Nature Physics **17**, 260 (2021).
- [9] G. Kokot, H. A. Faizi, G. E. Pradillo, A. Snezhko, and P. M. Vlahovska, Communications Physics **5**, 1 (2022).
- [10] Q. Roveillo, J. Dervaux, Y. Wang, F. Rouyer, D. Zanchi, L. Seuront, and F. Elias, Journal of the Royal Society Interface **17**, 20200077 (2020).
- [11] R. Di Leonardo, D. Dell'Arciprete, L. Angelani, and V. Iebba, Physical Review Letters **106**, 038101 (2011).
- [12] M. Morse, A. Huang, G. Li, M. R. Maxey, and J. X. Tang, Biophysical journal **105**, 21 (2013).
- [13] A. J. Mathijssen, A. Doostmohammadi, J. M. Yeomans, and T. N. Shendruk, Journal of The Royal Society Interface **13**, 20150936 (2016).
- [14] S. S. Suarez and A. Pacey, Human reproduction update **12**, 23 (2006).
- [15] D. Lopez and E. Lauga, Physics of Fluids **26**, 400 (2014).
- [16] Y. Alapan, U. Bozuyuk, P. Erkoc, A. C. Karacakol, and M. Sitti, Science robotics **5**, eaba5726 (2020).
- [17] B. Kavčič, D. Babič, N. Osterman, B. Podobnik, and I. Poberaj, Applied Physics Letters **95**, 023504 (2009).
- [18] F. Martinez-Pedrero and P. Tierno, Phys. Rev. Applied **3**, 051003 (2015).
- [19] F. Martínez-Pedrero and P. Tierno, Journal of colloid and interface science **519**, 296 (2018).
- [20] M. Driscoll and B. Delmotte, Current Opinion in Colloid & Interface Science (2018).
- [21] A. Chamolly, E. Lauga, and S. Tottori, Soft matter **16**, 2611 (2020).
- [22] X. Qi, S. Wang, S. Ma, K. Han, X. Bian, and X. Li, Physics of Fluids **33**, 121908 (2021).
- [23] U. Bozuyuk, E. Suadiye, A. Aghakhani, N. O. Dogan, J. Lazovic, M. E. Tiryaki, M. Schneider, A. C. Karacakol, S. O. Demir, G. Richter, *et al.*, Advanced Functional Materials **32**, 2109741 (2022).
- [24] A. F. Demirörs, A. Stauffer, C. Lauener, J. Cossu, S. N. Ramakrishna, J. De Graaf, C. C. Alcantara, S. Pané, N. Spencer, and A. R. Studart, Soft Matter **17**, 1037 (2021).
- [25] F. Martinez-Pedrero, E. Navarro-Argemí, A. Ortiz-Ambriz, I. Pagonabarraga, and P. Tierno, Science advances **4**, eaap9379 (2018).
- [26] B. Delmotte, Physical Review Fluids **4**, 044302 (2019).
- [27] F. Martinez-Pedrero, A. Ortiz-Ambriz, I. Pagonabarraga, and P. Tierno, Physical review letters **115**, 138301 (2015).
- [28] B. Sprinkle, E. B. Van Der Wee, Y. Luo, M. M. Driscoll, and A. Donev, Soft Matter **16**, 7982 (2020).
- [29] G. Junot, A. Cebers, and P. Tierno, Soft Matter **17**, 8605 (2021).
- [30] B. Delmotte, M. Driscoll, P. Chaikin, and A. Donev, Physical Review Fluids **2**, 092301 (2017).
- [31] B. Delmotte, A. Donev, M. Driscoll, and P. Chaikin, Physical Review Fluids **2**, 114301 (2017).
- [32] M. Driscoll, B. Delmotte, M. Youssef, S. Sacanna, A. Donev, and P. Chaikin, Nature Physics (2016).
- [33] J. W. Swan and J. F. Brady, Physics of Fluids (1994-present) **19**, 113306 (2007).
- [34] J. Blake and A. Chwang, Journal of Engineering Mathematics **8**, 23 (1974).
- [35] S. Lee, R. Chadwick, and L. G. Leal, Journal of Fluid Mechanics **93**, 705 (1979).
- [36] S. Kim and S. J. Karrila, *Microhydrodynamics: principles and selected applications* (Butterworth-Heinemann, Boston, 1991).
- [37] see Supplementary Information [url], .
- [38] W. Fei, P. M. Tzelios, and K. J. Bishop, Langmuir (2020).
- [39] C. Maldarelli, N. T. Donovan, S. C. Ganesh, S. Das, and J. Koplik, Annual Review of Fluid Mechanics **54**, 495 (2022).

Supplementary Materials

to

Viscosity ratio across interfaces controls the stability and self-assembly of microrollers

Blaise Delmotte*

LadHyX, CNRS, Ecole Polytechnique,

Institut Polytechnique de Paris, 91120 Palaiseau, France

I. FAR-FIELD APPROXIMATION OF THE SELF-INDUCED VELOCITY OF A SINGLE MICROROLLER ABOVE A FLUID-FLUID INTERFACE

The flow induced by a particle located at \mathbf{x}' and driven by a torque $\boldsymbol{\tau}$ is given by

$$\mathbf{u}(\mathbf{x}) = \frac{1}{2} [\nabla_{\mathbf{x}'} \times \mathbf{G}(\mathbf{x} - \mathbf{x}')] \cdot \boldsymbol{\tau} \quad (\text{S1})$$

where $\mathbf{G}(\mathbf{x} - \mathbf{x}') = 1/(\xi + 1)\mathbf{G}^{FS}(\mathbf{x} - \mathbf{x}') + \xi/(\xi + 1)\mathbf{G}^W(\mathbf{x} - \mathbf{x}')$ is the Green's function of the domain (Eq. (1) in the main text). The self-induced velocity \mathbf{v}_0 of the particle due to its own flow is given by the Faxen formula

$$\mathbf{v}_0 = \left(1 + \frac{a^2}{6}\nabla^2\right) \mathbf{u}(\mathbf{x}) \Big|_{\mathbf{x}=\mathbf{x}'} . \quad (\text{S2})$$

Using the analytical expressions of \mathbf{G}^{FS} and \mathbf{G}^W provided in [1] and [2] respectively, the self-induced response to an external torque aligned along the y -axis, $\boldsymbol{\tau} = \tau \mathbf{e}_y$, is given by $\mathbf{v}_0 = v_0 \mathbf{e}_x$ where

$$v_0 = \frac{\tau}{32\pi\eta a^2} \left(\frac{a}{h}\right)^2 \left[-\frac{1}{\xi + 1} + \frac{\xi}{\xi + 1} \frac{1}{2} \left(\frac{a}{h}\right)^2 \right], \quad (\text{S3})$$

which leads to Eq. (2) in the main text after normalizing by $\tau/8\pi\eta a^2$. Note that the self-induced velocity is always negative in the point-particle limit ($a/h \rightarrow 0$)

$$\lim_{a/h \rightarrow 0} v_0 = -\frac{\tau}{32\pi\eta} \frac{1}{\xi + 1} \frac{1}{h^2} \leq 0 \quad (\text{S4})$$

* blaise.delmotte@cnrs.fr

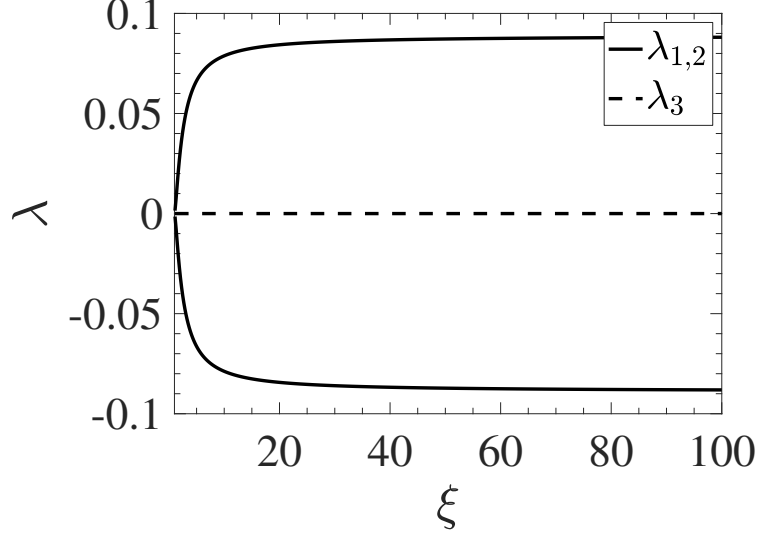


FIG. S1. Eigenvalues of $\nabla_{\mathbf{x}}\mathcal{G}(\mathbf{x})|_{\mathbf{x}_{\pm}^*}$ as a function of the viscosity ratio $\xi \in [1, 100]$

II. DYNAMICAL SYSTEM APPROACH FOR THE TWO POINT-TORQUES (ROTLETS)

A. Equations of motion

Consider two point particles with positions $\mathbf{x} = (x_i, z_i)$, $i = 1, 2$ driven by a torque $\boldsymbol{\tau}$ in the (x, z) -plane above a fluid-fluid interface. Since the particles have no size, the velocity of particle 1 due to the torque on particle 2 is equal to the fluid velocity at the particle position \mathbf{x}_1 :

$$\mathbf{v}_1 = \mathbf{u}_2(\mathbf{x} = \mathbf{x}_1) = \frac{1}{2} [\nabla_{\mathbf{x}'} \times \mathbf{G}(\mathbf{x}_1 - \mathbf{x}')]|_{\mathbf{x}'=\mathbf{x}_2} \cdot \boldsymbol{\tau} \quad (\text{S5})$$

From this formula, and by adding the self-induced contribution (S4), one obtains simple analytical expressions for the particle velocities $\mathbf{v}_i = (\dot{x}_i, \dot{z}_i)$, $i = 1, 2$. Using the translational invariance of the system along the x -direction, one can reduce the system to three degrees of freedom, $(x_{12} = x_1 - x_2, z_{12} = z_1 - z_2, z_C = (z_1 + z_2)/2)$, which leads to Eq. (3) in the main text.

B. Critical saddle points

The critical points of the dynamical system are found by solving

$$\begin{bmatrix} \dot{x}_{12} \\ \dot{z}_{12} \\ \dot{z}_C \end{bmatrix} = \begin{bmatrix} 2z_{12} \left(\frac{1}{r_{12}^3} - \frac{\xi}{\xi+1} \frac{2x_{12}^2 - 4z_C^2}{R_{12}^5} \right) - \frac{1}{4} \frac{1}{\xi+1} \left(\frac{1}{(z_C + z_{12}/2)^2} - \frac{1}{(z_C - z_{12}/2)^2} \right) \\ 2x_{12} \left(\frac{1}{R_{12}^3} - \frac{1}{r_{12}^3} + \frac{\xi}{\xi+1} \frac{12z_C^2}{R_{12}^5} \right) \\ \frac{\xi}{\xi+1} \frac{6x_{12}z_{12}z_C}{R_{12}^5} \end{bmatrix} = \mathcal{G}(\mathbf{x}) = \mathbf{0} \quad (\text{S6})$$

where $\mathcal{G}(\mathbf{x})$ is the vector field that describes the body dynamics in phase space. Their coordinate is given by $\mathbf{x}_\pm^* = (x_{12} = \pm x_{12}^*, z_{12} = 0, z_C = 1)$, where $x_{12}^* \neq 0$ is a zero of $\dot{z}_{12}(x_{12}, 0, 1, \xi)$, which is found by solving

$$x_{12}^3 \left(x_{12}^2 + 4 + 12 \frac{\xi}{\xi+1} \right) - (x_{12}^2 + 4)^{5/2} = 0. \quad (\text{S7})$$

In order to characterize these fixed points, we compute the eigenvalues of the Jacobian matrix of the system evaluated at \mathbf{x}^* ($\nabla_{\mathbf{x}} \mathcal{G}(\mathbf{x})|_{\mathbf{x}_\pm^*}$). Fig. S1 shows these eigenvalues as a function of $\xi \in [1, 100]$ (remember that the critical points do not exist for $\xi < 1$, see main text). Two eigenvalues are real with opposite signs and the third one is zero, which clearly shows that these critical points are saddle points and that the dynamics lies on a two-dimensional manifold in the vicinity of \mathbf{x}_\pm^* in phase space. These two saddle points with symmetric positions delimit a separatrix between periodic and non-periodic orbits. Since x_{12}^* decreases when ξ increases, the size of the domain enclosed by the separatrix decreases as well. Note that the magnitude of the eigenvalues increases with ξ , which indicates an acceleration of the relative motion between particles with ξ in the vicinity of the fixed points.

III. DETAILS ON THE LARGE SCALE 3D STOKESIAN DYNAMICS SIMULATIONS

Consider a collection of N microrollers with radius a and positions $\mathbf{X} = \{\mathbf{x}_1, \dots, \mathbf{x}_N\}$ subject external forces $\mathbf{F} = \{\mathbf{f}_1, \dots, \mathbf{f}_N\}$ and torques $\mathbf{T} = \{\boldsymbol{\tau}_1, \dots, \boldsymbol{\tau}_N\}$, where $\boldsymbol{\tau}_1 = \dots = \boldsymbol{\tau}_N = \boldsymbol{\tau} = \tau \mathbf{e}_y$. The equation of motion of the particles follow the mobility problem:

$$\dot{\mathbf{X}} = \mathbf{V} = \mathbf{M}^{VF} \cdot \mathbf{F} + \mathbf{M}^{VT} \cdot \mathbf{T} \quad (\text{S8})$$

where \mathbf{M}^{VF} and \mathbf{M}^{VT} are the mobility matrices that relate the particle velocities to their external forces and torques respectively. Similarly to Section I, they are obtained by applying

the Faxen laws to the flow induced by the particles above the interface, see [3, 4] for more details on their calculation. This modelling includes only leading-order corrections for the finite size of the particle to limit the computational cost required to simulate large numbers ($O(10^4)$) of particles. Even though this low-resolution model overestimates the particle mobility, our previous work shows that it reproduces qualitatively well the experimental results above a no-slip boundary [4–6].

The external force on each microroller \mathbf{f}_i is the resultant of a short-ranged repulsion between particles \mathbf{f}_P , a short range repulsion with the interface \mathbf{f}_I to avoid overlaps, and gravity \mathbf{f}_G , so that $\mathbf{f}_i = \mathbf{f}_P + \mathbf{f}_I + \mathbf{f}_G$. The short range repulsive forces \mathbf{f}_P and \mathbf{f}_I derive from an exponentially decaying repulsive potential of the form [5]

$$U(r) = \begin{cases} U_0(1 + \frac{d-r}{b}) & \text{if } r < d, \\ U_0 \exp(\frac{d-r}{b}) & \text{if } r \geq d. \end{cases} \quad (\text{S9})$$

For particle-particle interactions, r is the center-to-center distance and $d = 2a$. For particle-interface interactions, r is the height of the particle center and $d = a$. The energy scale U_0 and interaction range b control the strength and decay of the potential respectively. We found that taking $b = 0.1a$, $U_0 = \tau/2$ for particle-interface interactions and $b = 0.1a$, $U_0 = \tau/26$ for particle-particle interactions prevents overlaps while keeping close contact.

In the large scale particle simulations, a small amount of gravity is added: $\mathbf{f}_G = -mg\mathbf{e}_z$, with $mg = 0.0015\tau/a$. This is done because, in the absence of gravity, the front particles are lifted up quite high by the rear particles when $\xi = +\infty$. As a result, the transverse instability would take a long time to develop and, because it is proportional to the particle height [4, 5, 7], the wavelength of the instability would be large and becomes similar to the domain size. The addition of a small gravitational force slightly reduces the height of the front particles and therefore increases the growth rate of the instability and allows to have several wavelengths along the domain. However, the effects of gravity remain negligible compared to the torque induced flows ($\tau \gg mga$) and we have carefully checked that it did not change the qualitative behaviour of the suspension for all the values of ξ simulated.

Particle trajectories (S8) are integrated with the two-step Adams–Bashforth scheme. Mobility-vector products and steric interactions are computed with PyCUDA on an Nvidia Titan V GPU. The typical simulation time is 30 min for 4,000 time iterations with 10,000 particles.

IV. TWO-LINES MODEL

This section describes the two-line model and the details of the linear stability analysis. This model has already been used to describe the transverse instability of micro-rollers above a no-slip wall [7]. The derivation and analysis below are a direct extension of this work, where only the Green's function has been changed. For the sake of clarity we recall the governing equations and the main steps of the stability analysis.

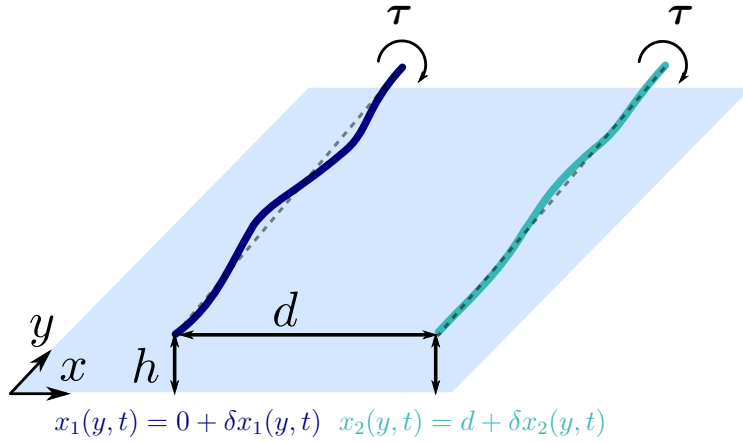


FIG. S2. Sketch of the two infinite lines. The rotlet densities are rotating with a constant torque, τ , about the y -axis and interact hydrodynamically in the xy -plane at a height h above the floor.

A. Governing equations

Consider two infinite lines of rotlets, labelled \mathcal{L}_1 , at the rear, and \mathcal{L}_2 , at the front, rotating around the y axis at a fixed height h in a plane parallel to the fluid-fluid interface (see Fig. S2). We denote $x_1(y, t)$ and $x_2(y, t)$ their position and $\rho_1(y, t) \equiv \rho(x_1(y, t), y, t)$ and $\rho_2(y, t) \equiv \rho(x_2(y, t), y, t)$ their rotlet densities. Here, we neglect out of plane motion in the z -direction and only consider the velocities in the xy -plane. Although out of plane motion is seen in 3D simulations, our previous work [4, 7] shows that the fingering instability still occurs when considering particles confined to a plane above the surface.

The model is governed by the equations of motion of each line together with the conservation

of rotlets along their length:

$$\begin{aligned}\frac{\partial x_i(y, t)}{\partial t} &= u_x(x_i(y, t), y) \\ \frac{\partial \rho_i(y, t)}{\partial t} &= -\frac{\partial[\rho_i(y, t)u_y(x_i(y, t), y)]}{\partial y}, \quad i = 1, 2,\end{aligned}\tag{S10}$$

where length and time have been rescaled with $l_c = h$ and $t_c = 8\pi\eta l_c^3/\tau$ respectively. These four PDEs are nonlinear and nonlocal. The velocity at a given point (x_i, y) along a line \mathcal{L}_i is given by the sum of the flows induced by each line,

$$u_x(x_i, y) = \sum_{j=1}^2 \int_{-\infty}^{+\infty} \mu_x^{u\tau}(x_i - x_j, y - y') \rho_j(y') dy', \tag{S11}$$

$$u_y(x_i, y) = \sum_{j=1}^2 \int_{-\infty}^{+\infty} \mu_y^{u\tau}(x_i - x_j, y - y') \rho_j(y') dy', \tag{S12}$$

where $\mu^{u\tau}(\mathbf{x} - \mathbf{x}')$ is the operator which provides the fluid velocity in the plane at position $\mathbf{x} = (x, y, h)$ induced by a rotlet at position $\mathbf{x}' = (x', y', h)$. It is given by

$$\mu_x^{u\tau}(x - x', y - y') = 1/2 [(\nabla_{\mathbf{x}'} \times \mathbf{G}(x - x', y - y'; h)) \cdot \mathbf{e}_y] \cdot \mathbf{e}_x \tag{S13}$$

$$= \frac{\xi}{\xi + 1} 6h^3 \frac{(x - x')^2}{R^5} - \frac{1}{\xi + 1} 2 \frac{h^3}{R^3} \tag{S14}$$

$$= \frac{\xi}{\xi + 1} u_x^W + \frac{1}{\xi + 1} u_x^{FS} \tag{S15}$$

$$\mu_y^{u\tau}(x - x', y - y') = 1/2 [(\nabla_{\mathbf{x}'} \times \mathbf{G}(x - x', y - y'; h)) \cdot \mathbf{e}_y] \cdot \mathbf{e}_y \tag{S16}$$

$$= \frac{\xi}{\xi + 1} 6h^3 \frac{(x - x')(y - y')}{R^5} + \frac{1}{\xi + 1} \times 0 \tag{S17}$$

$$= \frac{\xi}{\xi + 1} u_y^W + \frac{1}{\xi + 1} u_y^{FS} \tag{S18}$$

where $R = [(x - x')^2 + (y - y')^2 + 4h^2]^{1/2}$. As shown on Figure S3 the free-surface contribution has no transverse flow: $u_y^{FS} = 0$.

B. Linear stability analysis

The base state of this system corresponds to two straight lines with uniform rotlet densities ($\rho_i(y, t) = \rho_0$) translating at a steady speed, so that their position are constant in the moving frame ($x_1(y, t) = 0$, $x_2(y, t) = d$), where d is the initial distance between the two lines.

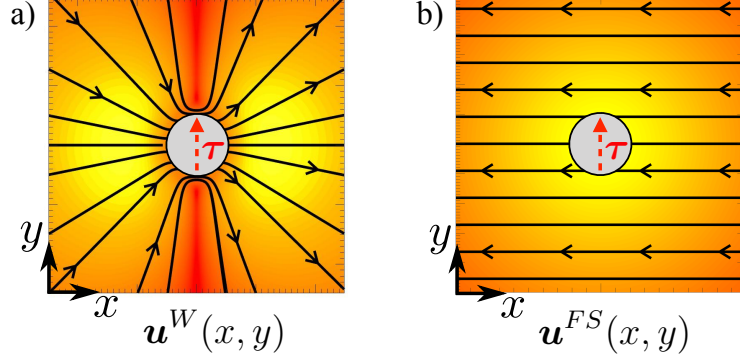


FIG. S3. Flow induced by a microroller in the plane parallel to the surface. a) No-slip wall (W), b) Free-surface (FS).

We perturb the system about the base state

$$x_1(y, t) = 0 + \delta x_1(y, t) \quad (\text{S19})$$

$$x_2(y, t) = d + \delta x_2(y, t), \quad (\text{S20})$$

$$\rho_1(y, t) = \rho_0 + \delta \rho_1(y, t) \quad (\text{S21})$$

$$\rho_2(y, t) = \rho_0 + \delta \rho_2(y, t), \quad (\text{S22})$$

where $\delta x_1, \delta x_2 \ll \min(d, h)$ and $\delta \rho_1, \delta \rho_2 \ll \rho_0$.

After Taylor expanding the functionals in Eqs. (S10)-(S12) we obtain the linearized governing equations

$$\frac{\partial \delta x_1}{\partial t} = \rho_0 \mathcal{G}_0 \delta x_1 + \rho_0 \mathcal{G}_1 * \delta x_2 + \mu_x^{u\tau} (0 - d, \cdot) * \delta \rho_2 \quad (\text{S23})$$

$$\frac{\partial \delta x_2}{\partial t} = -\rho_0 \mathcal{G}_0 \delta x_2 - \rho_0 \mathcal{G}_1 * \delta x_1 + \mu_x^{u\tau} (0 - d, \cdot) * \delta \rho_1 \quad (\text{S24})$$

$$\frac{\partial \delta \rho_1}{\partial t} = -\rho_0 \frac{\partial [(\rho_0 \mathcal{G}_2 * \delta x_1 + \rho_0 \mathcal{G}_3 * \delta x_2 + \mu_y^{u\tau} (0 - d, \cdot) * \delta \rho_2)]}{\partial y} \quad (\text{S25})$$

$$\frac{\partial \delta \rho_2}{\partial t} = -\rho_0 \frac{\partial [(\rho_0 \mathcal{G}_2 * \delta x_2 + \rho_0 \mathcal{G}_3 * \delta x_1 - \mu_y^{u\tau} (0 - d, \cdot) * \delta \rho_1)]}{\partial y}, \quad (\text{S26})$$

where we have used the symmetries of $\mu_x^{u\tau}$ and $\mu_y^{u\tau}$. The star “*” denotes the one dimensional

convolution product. The interaction kernels are given by

$$\begin{aligned}\mathcal{G}_0 &= \frac{\partial}{\partial x_1} \left[\int_{-\infty}^{+\infty} \mu_x^{u\tau}(x_1 - d, y - y') dy' \right] \Big|_{x_1=0} \\ \mathcal{G}_1(y - y') &= \frac{\partial \mu_x^{u\tau}(0 - x_2, y - y')}{\partial x_2} \Big|_{x_2=d}, \\ \mathcal{G}_2(y - y') &= \frac{\partial \mu_y^{u\tau}(0 - x_1, y - y')}{\partial x_1} \Big|_{x_1=0}, \\ \mathcal{G}_3(y - y') &= \frac{\partial \mu_y^{u\tau}(0 - x_2, y - y')}{\partial x_2} \Big|_{x_2=d}.\end{aligned}$$

Note that \mathcal{G}_0 is a constant which depends only on the geometric parameters of the problem d, h .

Looking for periodic solutions of Eqs. (S23)-(S26) of the form

$$\mathbf{u} = (\delta x_1, \delta x_2, \delta \rho_1, \delta \rho_2) = \tilde{\mathbf{u}} e^{iky + \sigma t},$$

where the wavenumber $k = 2\pi/\lambda$ and

$$\tilde{\mathbf{u}} = (\delta \tilde{x}_1, \delta \tilde{x}_2, \delta \tilde{\rho}_1, \delta \tilde{\rho}_2),$$

we obtain the following eigenvalue problem

$$A\tilde{\mathbf{u}} = \sigma\tilde{\mathbf{u}} \tag{S27}$$

where

$$A = \begin{bmatrix} \rho_0 \mathcal{G}_0 & \rho_0 \tilde{\mathcal{G}}_1 & 0 & \tilde{\mu}_x^{u\tau}(-d, k) \\ -\rho_0 \tilde{\mathcal{G}}_1 & -\rho_0 \mathcal{G}_0 & \tilde{\mu}_x^{u\tau}(-d, k) & 0 \\ -ik\rho_0^2 \tilde{\mathcal{G}}_2 & -ik\rho_0^2 \tilde{\mathcal{G}}_3 & 0 & -ik\rho_0 \tilde{\mu}_y^{u\tau}(-d, k) \\ -ik\rho_0^2 \tilde{\mathcal{G}}_3 & -ik\rho_0^2 \tilde{\mathcal{G}}_2 & ik\rho_0 \tilde{\mu}_y^{u\tau}(-d, k) & 0 \end{bmatrix}, \tag{S28}$$

and the tilde denotes the Fourier transform with respect to y , e.g.

$$\tilde{\mu}_x^{u\tau}(-d, k) = \int_{-\infty}^{\infty} \mu_x^{u\tau}(-d, y) \exp(-iky) dy. \tag{S29}$$

For the sake of conciseness, the exact expressions of the entries of A are not reported here. They correspond to linear combinations of the expressions given in the main text

and appendix A of [7]. Due to the particular structure of A , Eq. (S27) can be solved analytically. The four solutions $\sigma_1(k, \xi), \dots, \sigma_4(k, \xi)$ are given by

$$\begin{aligned} \sigma_{1,2,3,4}(k, \xi) = & \pm \frac{1}{2} \left[2A_{11}^2 - 2A_{12}^2 + 4A_{32}A_{14} - 2A_{34}^2 \right. \\ & \pm 2 \left(A_{11}^4 - 2A_{11}^2A_{12}^2 + 4A_{11}^2A_{14}A_{32} + 2A_{11}^2A_{34}^2 - 8A_{11}A_{14}A_{31}A_{34} + A_{12}^4 \right. \\ & \left. \left. - 4A_{12}^2A_{14}A_{32} - 2A_{12}^2A_{34}^2 + 8A_{12}A_{14}A_{32}A_{34} + 4A_{14}^2A_{31}^2 - 4A_{14}A_{32}A_{34}^2 + A_{34}^4 \right)^{1/2} \right]^{1/2}. \end{aligned} \quad (\text{S30})$$

The first two eigenvalues are real and of opposite sign $\sigma_1 = -\sigma_2$. The two other are imaginary and conjugate $\sigma_3 = \bar{\sigma}_4$. Figure 3b in the main text shows the positive real eigenvalue σ_1 , i.e. the unstable one, for $d = 10h$.

V. DETAILS ON THE MEAN-FIELD SIMULATIONS

The nonlocal mean-field equations Eq. (6)-(7) in the main text are solved numerically with a third-order second-time finite volume method optimally designed for hyperbolic scalar conservation equations [8, 9]. The rectangular computational domain is discretized with a cartesian grid with cell sizes Δx and Δz respectively. The domain dimensions L_x and L_z are chosen to ensure that the roller density remains small at the boundaries ($\rho/\rho_0 < \epsilon = 10^{-4}$) during the simulation time. The time step Δt is automatically chosen at each time iteration to ensure that the CFL condition is always satisfied: $\Delta t = 0.9 \min(\Delta x/u_x, \Delta z/u_z)$. The integrals in Eq. (7) in the main text are evaluated with a Riemann sum using PyCUDA on an Nvidia Titan V GPU for efficiency. The typical simulation time is 50 min for 9,000 time iterations with $N = N_x \times N_z = 1500 \times 200 = 3 \cdot 10^5$ grid cells.

Note that corrections for the finite size of the particles could be included in the hydrodynamic interactions in Eq. (7) (as done in the particle simulations) with no additional complexity, but these effects are negligible at the macroscopic level where collective effects dominate at large scales.

VI. MOVIE CAPTIONS

- SI Movie 1, “Particle_simulations_compare_xi_top_view.avi”: Top view of the time-evolution of 10,000 microrollers initially uniformly distributed in a monolayer above the interface. Each color, from dark blue to yellow, corresponds to a different value of $\xi \in \{0, 0.5, 1.5, 5, +\infty\}$ simulated independently with the 3D Stokesian Dynamics approach.
- SI Movie 2, “Particle_simulations_compare_xi_side_view.avi”: Side view of the numerical simulations shown in SI Movie 1.
- SI Movie 3, “Continuum_model_xi_0.mp4”: numerical simulation of the continuum model above an interface with viscosity ratio $\xi = 0$ (free-slip). The rollers are initially uniformly distributed ($\rho/\rho_0 = 1$) over a thin strip of aspect ratio $\gamma = L/H = 9.4$ near the interface. Colorbar: normalized particle density ρ/ρ_0 . Black arrow: fluid velocity field. The boundary of the cluster is defined by the green isocontour $\rho/\rho_0 = 0.4$. The motion along the x -axis is expressed relative to the initial position of the center of mass, $x_C^0 = x_C(t = 0)$, in order to show how far the cluster has travelled at the end of the simulation.
- SI Movie 4, “Continuum_model_xi_0.5.mp4”: same as SI Movie 3 but with $\xi = 0.5$.
- SI Movie 5, “Continuum_model_xi_1.1.mp4”: same as SI Movie 3 but with $\xi = 1.1$.
- SI Movie 6, “Continuum_model_xi_5.0.mp4”: same as SI Movie 3 but with $\xi = 5$.
- SI Movie 7, “Continuum_model_xi_infty.mp4”: same as SI Movie 3 but with $\xi = +\infty$ (no-slip wall).

-
- [1] S. Lee, R. Chadwick, and L. G. Leal, Motion of a sphere in the presence of a plane interface. part 1. an approximate solution by generalization of the method of lorentz, *Journal of Fluid Mechanics* **93**, 705 (1979).
- [2] J. Blake and A. Chwang, Fundamental singularities of viscous flow, *Journal of Engineering Mathematics* **8**, 23 (1974).

- [3] J. W. Swan and J. F. Brady, Simulation of hydrodynamically interacting particles near a no-slip boundary, *Physics of Fluids* (1994-present) **19**, 113306 (2007).
- [4] M. Driscoll, B. Delmotte, M. Youssef, S. Sacanna, A. Donev, and P. Chaikin, Unstable fronts and motile structures formed by microrollers, *Nature Physics* (2016).
- [5] F. B. Usabiaga, B. Delmotte, and A. Donev, Brownian dynamics of confined suspensions of active microrollers, *J. Chem. Phys.* **146**, 134104 (2017), software available at <https://github.com/stochasticHydroTools/RigidMultiblobsWall>.
- [6] B. Delmotte, M. Driscoll, P. Chaikin, and A. Donev, Hydrodynamic shocks in microroller suspensions, *Physical Review Fluids* **2**, 092301 (2017).
- [7] B. Delmotte, A. Donev, M. Driscoll, and P. Chaikin, Minimal model for a hydrodynamic fingering instability in microroller suspensions, *Physical Review Fluids* **2**, 114301 (2017).
- [8] J. B. Bell, C. N. Dawson, and G. R. Shubin, An unsplit, higher order godunov method for scalar conservation laws in multiple dimensions, *Journal of Computational Physics* **74**, 1 (1988).
- [9] S. May, A. Nonaka, A. Almgren, and J. Bell, An unsplit, higher-order godunov method using quadratic reconstruction for advection in two dimensions, *Communications in Applied Mathematics and Computational Science* **6**, 27 (2011).